Quasi-particle energies and optical excitations of ZnS monolayer honeycomb structure

Article *in* Applied Surface Science · August 2016

DOI: 10.1016/j.apsusc.2016.08.055

CITATIONS
18

READS
241

1 author:

Masoud Shahrokhi
ICIQ Institute of Chemical Research of Catalonia
54 PUBLICATIONS **398** CITATIONS

SEE PROFILE

Quasi-particle energies and optical excitations of ZnS monolayer honeycomb structure

Masoud SHAHROKHI*

Université Paris-Est, Laboratoire Modélisation et Simulation Multi Echelle, MSME UMR 8208 CNRS, 5 bd Descartes, F-77454 Marne-la-Vallée, France

Corresponding author:

*corresponding author. Tel.: +33.1.60.95.73.84

E-mail address: shahrokhimasoud37@gmail.com. (Masoud Shahrokhi)

Abstract

Using *ab-initio* density functional theory calculations combined with many-body perturbation formalism we carried out the electronic structure and optical properties of 2D graphene-like ZnS structure. The electronic properties were analyzed at three levels of many-body GW approach (G_0W_0, GW_0 and GW) constructed over a Generalized Gradient Approximation functional. Our results indicate that ZnS sheet has a direct band gap at the Γ-point. Also it is seen that inclusion of electron-electron interaction does not change the sort of direct semiconducting band gap in ZnS sheet. The optical properties and excitonic effects of these materials are investigated using the Bethe-Salpeter equation (BSE) approach. The formation of first exciton peaks at 3.86, 4.26, and 4.57 eV with large binding energy of 0.36, 0.49 and 0.73 eV using G_0W_0+BSE, GW_0+BSE and GW+BSE, respectively, was observed. We show that the optical absorption spectrum of 2D ZnS structure is dominated by strongly bound Frenkel excitons. The enhanced excitonic effects in the ZnS monolayer sheet can be useful in designing optoelectronic applications.

1. Introduction

Zn-VI-based semiconductors have captivated enormous significant amount of attention due to their applications in short-wavelength light-emitting devices [1-3]. Due to these powerful applications, a number of studies have been devoted to exploring new possible structural phases for these semiconductors especially in nanocrystalline form [4-11]. Among the family of Zn–VI

semiconductors, ZnS with two different crystal structures (zinc blende and wurtzite) [4] is a commercially important semiconductor having a wide direct band gap (E_g =3.68 eV) [12], rendering it a very attractive material for optical application. ZnS has important applications in ultraviolet light-emitting diodes and injection lasers [13], flat panel displays [14], sensors[15], infrared optical windows [16], photocatalysis and triboluminescence [17].

In a recent articles by Akhtar *et al.* [18-20], full-potential linearized augmented plane wave (FP-L/APW) method based on spin-polarize DFT was employed to investigate the electronic and magnetic properties of transition metal atoms (TM) doped ZnS thin film. Electronic band structures and density of states (DOS) of these compounds demonstrate 100% spin polarization (half metallicity) with ferromagnetic exchange interactions. These ZnS based half metallic ferromagnets have the potential applications in future spintronic devices. Furthermore, the ZnS films show high crystallinity, good adhesion and minimum reflection in the visible region and hence have potential applications in optoelectronic or solar cell devices [21]. Several researchers have previously investigated the electronic, magnetic, optical and mechanical properties of nanostructures of ZnS including nanotubes, nanowires, nanobelts, and monolayer hexagonal sheets [12-16, 22, 23]. It is found that the band gap of ZnS nanostructures is smaller than that of SiC [24], BN [25] and BeO [26-28] nanostructures. Theoretical studies predict that the ZnS monolayers have planar and buckled structures [29]. Also, a few theoretical studies have reported the electronic band structure, real and imaginary parts of the dielectric function and energy-loss spectra of monolayer 2D-graphene like ZnS sheet [3, 29, 30]. In all those theoretical studies, the electronic and optical properties have been investigated using the density functional theory (DFT) [31] and random phase approximation (RPA) [32]. Concerning the calculation of the electronic and optical properties of semiconductors and insulators, the DFT and RPA are not sufficient to yield results in quantitative agreement with experiments because they ignore many-body effects on electronic and optical properties. The many-body GW approximation (GWA) provides a correct description of the electronic structure around the gap, in contrast to the DFT, which leads to more accurate band gaps in the semiconductors and insulators [33-35]. Moreover, the electron-hole two-particle Green function in Bethe-Salpeter equation approach (BSE) [36] allows to develop the optical response of a system.

The objective of this paper is to evaluate the many-body effects on the electronic and optical properties of 2D-graphene like ZnS. Systematic studies of these properties, such as predicted band gap values, using various levels of GWA on these materials are reported. GWA calculations were performed at three levels. First we used single shot GW (usually called G_0W_0) which has a tendency toward too small gaps compared to experiment [34]. Since the best results for electronic band gap of semiconductors and insulators are obtained on the level of the GW_0 approximation [34], we also used GW_0 to obtain accurate estimation of band gap in both bulk and sheet systems. In GW_0 the eigenvalues in the Green's function G (GW_0) are updated until self-consistency is reached. At the end, GW calculations with a full update of the Green's function G and screened potential W carried out for GWA calculations. The optical spectra of the studied materials were modeled using the different level of GWA plus BSE approach, which includes both electron-electron (e-e) and electron-hole (e-h) correlation effects.

The paper is organized as follows: In next section, the details of the computational methods employed to compute the electronic and optical properties are presented. Section 3 covers the results related to electronic properties using G_0W_0, GW_0, and GW levels of many-body GWA in modeling the ZnS sheet. In section 4 optical properties, evaluated from BSE on top of GWA for the aforementioned material, are described and the role of excitonic effects is discussed. In the last section we summarize our studies and present the conclusion.

2. Computational details

In the present work, the ground state electronic properties of ZnS sheet calculated using the DFT by adopting the generalized gradient approximation of PBE functional [37] for the exchange correlation potential and the projector augmented wave (PAW) [38] method as implemented in the Vienna ab initio simulation package (Vasp) [39]. For the Brillouin zone integration, a 18×18×1 Γ centered Monkhorst-Pack k-point mesh is used to ensure converged structural and electronic results and 36×36×1 k-point grids are necessary for computing optical properties. Before electronic and optical calculations, ZnS sheet was optimized by a conjugate gradient method until the force component on every atom was less than 10^{-5} eV/Å. The quasi-particle (QP) energies in G_0W_0 approximation are obtained considering the Kohn-Sham eigenstates and eigenvalues as a starting point, which are solutions of

$$(T+V_{n-e}+V_H+V_{XC})\phi_{nk}=\phi_{nk}E_{nk} \quad (1)$$

where T is the kinetic-energy operator, V_{n-e} the potential of the nuclei, V_H the Hartree potential, V_{xc} the exchange-correlation energy, and n and k the band and k-point indices, respectively. Then, QP energies E_{nk}^{QP} can be calculated within the GWA as a first-order correction to the DFT single-particle energies E_{nk}

$$E_{nk}^{QP,1}=\mathrm{Re}[\left\langle \phi_{nk}\middle|T+V_{n-e}+V_H+\sum\nolimits_{XC}(G,W;E_{nk})\middle|\phi_{nk}\right\rangle] \quad (2)$$

In this equation, both Green' s function G and the screened Coulomb interaction W in the self-energy operator $\sum$ are calculated using the DFT single-particle energies and wave functions [33, 40]. The updated quasi-particle energy $E_{nk}^{QP,i+1}$ is then obtained from the quasi-particle energy at the previous iteration $E_{nk}^{QP,i}$ by linearization of Eq. (2) as follows [34]:

$$E_{nk}^{QP,i+1}=E_{nk}^{QP,i}+Z_{nk}\,\mathrm{Re}[\left\langle \phi_{nk}\middle|T+V_{n-e}+V_H+\sum\nolimits_{XC}(G,W;E_{nk}^{QP,i})\middle|\phi_{nk}\right\rangle-E_{nk}^{QP,i}] \quad (3)$$

where Z_{nk} is the renormalization factor [8],

$$Z_{nk}=\left(1-\mathrm{Re}\left\langle \phi_{nk}\middle|\frac{\partial}{\partial\omega}\sum\omega|_{E_{nk}^{QP,i}}\middle|\phi_{nk}\right\rangle\right)^{-1} \quad (4)$$

In the GW_0 case, Green's function G was iterated while the screened Coulomb potential W was kept fixed at the initial DFT value (W_0). In the GW case, W and dielectric matrix were reevaluated in each iteration using the new QP energies. The iterative process is generally carried out until self-consistency is reached. To obtain excellent converged results, we used four iterations in our calculations. The band gap value in GWA calculations is very sensitive to many parameters like k-point grid sampling of Brillouin Zone (BZ), thickness of vacuum layer, energy cutoffs for plane-wave calculations, number of bands for the expansion of Green's function and frequency grid. The GW and Bethe–Salpeter calculations in this paper converged with respect to

these parameters. A vacuum layer of 30 Å in the direction normal to the sheet plane was included to minimize any interactions between adjacent layers. In our calculations we employed 400 empty conduction bands in GWA calculations. However, the number of empty conduction bands was converged; there are some evidences that show this number is enough for GW and BSE calculations using Vasp. For example Karlicky *et al* [40] only used 64 empty bands to investigate band gaps and optical spectra of chlorographene, fluorographene and graphane using GWA and BSE. It is found that the band gap difference of single-layer graphene fluoride for 128 empty bands and 4096 empty bands is less than 0.05 eV [41]. The converged empty bands parameter used for MoS_2 monolayer is 96 bands [42]. Furthermore, 150 empty bands were employed to investigate GW calculations for bulk structure of semiconductors and insulators by Shishkin *et al* [34]. They showed that residual errors due to the number of unoccupied bands are expected to be of the order of 1% and 20 – 30 meV for semiconductors and insulators. In addition, 200 frequency grid points were employed in the GWA calculations. The response function was set with a cutoff energy of 300 eV. This parameter controls how many G-vectors are included in the response function. After calculation of the electronic ground states, optical properties like imaginary and real parts of dielectric function of the considered materials were investigated. The optical properties are determined by the dielectric function $\varepsilon(\omega) = \mathrm{Re}\,\varepsilon_{\alpha\beta}(\omega) + i\,\mathrm{Im}\,\varepsilon_{\alpha\beta}(\omega)$, which is mainly contributed from the electronic structures. The imaginary part $\mathrm{Im}\,\varepsilon_{\alpha\beta}(\omega)$ of the dielectric function could be obtained from the momentum matrix elements between the occupied and unoccupied wave functions [26, 43]

$$\mathrm{Im}\,\varepsilon_{\alpha\beta}(\omega) = \frac{4\pi^2 e^2}{\Omega}\lim_{q\to 0}\frac{1}{|q|^2}\sum_{c,v,k} 2w_k\,\delta(\varepsilon_{ck} - \varepsilon_{vk} - \omega)\times\left\langle u_{ck+e_\alpha q}\middle|u_{vk}\right\rangle\left\langle u_{ck+e_\beta q}\middle|u_{vk}\right\rangle^* \tag{5}$$

Where q is the Bloch vector of the incident wave and w_k the **k**-point weight. The band indices c and v are restricted to the conduction and the valence band states, respectively. The vectors e_α are the unit vectors for the three Cartesian directions and Ω is the volume of the unit cell. u_{ck} is the cell periodic part of the orbitals at the k-point **k**. The real part $\mathrm{Re}\,\varepsilon_{\alpha\beta}(\omega)$ can be evaluated from $\mathrm{Im}\,\varepsilon_{\alpha\beta}(\omega)$ using the Kramers–Kronig transformation [44]:

$$\mathrm{Re}\,\varepsilon_{\alpha\beta}(\omega) = 1 + \frac{2}{\pi} P \int_0^{\infty} \frac{\omega' \,\mathrm{Im}\,\varepsilon_{\alpha\beta}(\omega')}{(\omega')^2 - \omega^2 + i\eta} d\omega' \qquad (6)$$

Where P denotes the principle value and η is the complex shift in Kramers-Kronig transformation. In our calculations, we used η = 0.1 which is perfectly acceptable for most calculations and causes a slight smoothening of the real part of the dielectric function. Local field effects, which correspond to changes in the cell periodic part of the potential, were included in the random phase approximation. We compared optical properties calculated (i) without consider both electron–electron and electron-hole correlation, DFT+RPA [32], (ii) with electron-electron interaction included and electron-hole interactions neglected (RPA using the GW quasi-particle spectra), GW+RPA [33], and finally (iii) both electron-electron and electron-hole interactions, relevant in photo-excitation processes, are included by solving the Bethe-Salpeter equation (BSE) [36]. The electron-hole excited state was represented by the expansion [40]

$$|S\rangle = \sum_{c}^{elec} \sum_{v}^{hole} \sum_{k} A_{cvk}^{S} |cvk\rangle \qquad (7)$$

where A^S is the amplitude of a free electron-hole pair configuration composed of the electron state $|ck\rangle$ and the hole state $|vk\rangle$. A^S was obtained by diagonalization of the excitonic equation [45, 46] implemented also in VASP [47] according to Eq. 8, which corresponds to the BSE

$$(E_{ck}^{QP} - E_{vk}^{QP}) A_{cvk}^{S} + \sum_{c'v'k'} \langle cvk | K^{e-h} | c'v'k' \rangle A_{c,v,k}^{S} = \Omega^{S} A_{cvk}^{S} \qquad (8)$$

where E_{vk}^{QP} and E_{ck}^{QP} denote the quasi-particle eigenvalues of valence and conduction bands at a specific k-point, respectively. $K^{e\text{-}h}$ is the kernel describing the interaction between excited electrons and holes and A_{cvk}^{S}, Ω^{S} are the exciton eigenfunction and eigenvalue for the *S-th* exciton, respectively. The optical spectra within GW_0+BSE were calculated including 8 valence bands and 36 conduction bands.

3. Results and discussion

3.1. Electronic properties

Zinc and sulphide atoms in 2D graphene like structure are located in *x*-*y* plane with periodic boundary conditions with a vacuum space in *z*-axis to avoid the interactions between adjacent sheets. The top and side views of 2D- ZnS are shown in Fig. 1 (a) and (b), respectively. The optimized 2D hexagonal lattice constant and Zn-S bond length in ZnS sheet are 3.89 and 2.24 Å, which is close to previous calculation [12]. To investigate electronic properties of 2D graphene like ZnS, the band structure, total and partial density of states (DOS) are calculated and the obtained results from the PBE and different levels of GWA are compared. Fig. 2 (a) and (b) illustrate the band structure along the high symmetry *Γ*- *M*- *K*- *Γ* directions, total and partial DOS of ZnS sheet using PBE and G_0W_0 approaches, respectively. The both valence band maximum (VBM) and the conduction band minimum (CBM) of 2D graphene like ZnS occur at the *Γ*-point, resulting in a direct band gap. It is well visible that the nearest bands to VBM have main contribution from the S atom while above Fermi energy, nearest bands to CBM are mainly composed by Zn atom. Table 1 summarizes our results for the band gap values of ZnS sheet within PBE, G_0W_0, GW_0 and GW approaches. To compare we also reported others available theoretical results [3, 12, 30] in this table. Our results show that the band gap of ZnS sheet using PBE is 2.65 eV which is 0.12 eV smaller than previous PBE results [3]. As can be seen from Fig. 2 (b) the G_0W_0 approximation has led to a constant shift of the PBE bands: Unoccupied bands are moved to higher energies, whereas occupied bands are shifted down. Also it is seen that G_0W_0 technique does not change the sort of direct semiconducting band gap in ZnS sheet. The calculated direct band gap from G_0W_0 is 4.22 eV for ZnS sheet which is 1.57 eV larger than PBE value. This band gap increase is due to the electron-electron self-energy effects in the G_0W_0 approximation.

We also used GW_0 and GW approaches to obtain estimation of band gap in 2D graphene like ZnS system. Total DOS of ZnS sheet within the PBE, G_0W_0, GW_0 and GW approaches are shown in Fig. 2 (c). The calculated band gap using GW_0 and GW is 4.75 and 5.3 eV, respectively (Table 1). The QP band gaps for various approaches, follow the order of PBE < G_0W_0 < GW_0 < GW, similar to what was found for conventional main group semiconductors by Shishkin and

Kresse [34] and for MnO, CoO, and NiO comparing only G_0W_0 and GW_0 by Jiang *et al* [48]. We note that G_0W_0 approximation always yields small band gaps, GW_0 technique leads to excellent agreement with experiment and GW technique gives too large band gaps for virtually all materials [34]. However, to the best of our knowledge, there are no experimental results for the band gap of 2D-ZnS we believe our results of GW_0 band gap is completely reliable to compare with experiment.

The PBE and G_0W_0 partial electronic DOS (PDOS) of 2D-ZnS structure are shown in Fig. 3. PDOS of Zn and S atoms show a strong hybridization of Zn 3*d* and S 2*p* states in the valence band. It also can be seen that the nearest bands to the valance band below Fermi energy have main contribution from the S 2*p* states while above Fermi energy, nearest bands to the conduction band are mainly contributed by the Zn 4*s* states. The S 2*p* and Zn 4*s* states have a significant role to play in the lowest exciton peaks which will be discussed in the next section. The G_0W_0 approximation moves occupied bands of both Zn and S atoms to lower energies, while unoccupied bands of these atoms are moved to higher energies.

3.2. Optical properties

In this section applying the BSE method [36], the optical properties of 2D-ZnS, such as the dielectric function, exciton binding energy, exciton Bohr radius and electron energy-loss spectrum (EELS) are calculated. The optical spectra of the 2D graphene-like ZnS have been modeled using the different level of GWA plus BSE approach (accounting for both e-e and e-h effects). Since the best results for electronic band gap of semiconductors are obtained on the level of the GW_0 approach [34], we focus mainly on the optical spectra of the 2D graphene-like ZnS modeled using the GW_0 plus BSE approach. For a better comprehension of 2D-ZnS optical properties, the DFT+RPA (neglecting e-e and e-h correlations) and GW_0+RPA (e-e correlation included and e-h correlation neglected) results are also reported. Because of the huge depolarization effect in the 2D planar geometry for light polarization perpendicular to the plane ($E||z$ from Fig. 1) [49] we only focus on the optical absorption spectrum for light polarization parallel to the plane. Due to the symmetric structure of ZnS sheet, the optical spectra of this system are isotropic for light polarizations along the *x*-axis ($E||x$) and *y*-axis ($E||y$). Hence, the

optical properties for light polarizations along the *x*-axis are reported. The imaginary and real parts of dielectric function of ZnS sheet obtained using DFT+RPA, GW_0+RPA and GW_0+BSE are illustrated in Figure 4 (a) and (b), respectively. Comparison of the imaginary part of dielectric function obtained at the DFT+RPA and GW_0+RPA levels shows that inclusion of e-e interaction led to a blue shift; however, the global shape of the spectra was preserved. On the other hand, inclusion of e-h attraction (excitonic effects) in BSE yielded a significant red shift of $\mathrm{Im}\,\varepsilon_{\alpha\beta}(\omega)$. Furthermore, the most important physical effect of the e-h interactions was appearance of some bound excitons below the GW_0 gap, which were utterly missing in the GW_0+RPA. Inclusion of e-e interactions with GW_0+RPA decreased the static dielectric constant (the real part of dielectric constant at zero energy) compared with DFT+RPA. Whereas, when the e-h interactions were included, the static dielectric constant increased compared with GW_0+RPA (Fig. 4 (b)).

The lowest excitoinc within GW_0+BSE was observed at $E_0^{11} = 4.26$ eV, which presents a large binding energy of 0.49 eV and arises due to direct interband transitions involving the VBM and CBM at Γ (see Fig. 2 (b)). The second and third peaks, $E_1^{11} = 4.92$ eV and $E_2^{11} = 5.36$ eV, correspond to the first and second excited-state of exciton E_0^{11}, respectively. The second and third excited states become photoactivated at *M* and *K* wavevectors, respectively. These first three exciton peaks are due to electron transition from S 2*p* (valance band) to Zn 4*s* (conduction band) (see Fig. 3). Table 2 shows our results of the excitoinc peaks of ZnS sheet within GW_0+BSE approach. We also used G_0W_0+BSE and GW+BSE to obtain estimation of optical excitations of ZnS sheet. The imaginary and real parts of dielectric function of this system using the G_0W_0+BSE, GW_0+BSE and GW+BSE for light polarization parallel to the surface plane are shown in Fig. 5 (a) and (b), respectively. The positions of the first three exciton peaks were observed at $E_0^{11} = 3.86$ eV, $E_1^{11} = 4.60$ eV and $E_2^{11} = 4.95$ eV using G_0W_0+BSE, while these value are $E_0^{11} = 4.57$ eV, $E_1^{11} = 5.27$ eV and $E_2^{11} = 5.64$ eV for GW+BSE (Table 2).

The binding energy of the lowest energy exciton (E_B) was computed by,

$$E_B = E_g - E_{ex}$$

where E_g is the QP band gap and E_{ex} is excitation energy. Table 2 summarizes our results for the binding energy of first exciton values of ZnS sheet. The binding energy of the first exciton is 0.36, 0.49 and 0.73 eV within G_0W_0+BSE, GW_0+BSE and GW+BSE, respectively. The calculated binding energies for ZnS sheet is much larger than that found for excitons in Si and GaAs, corresponding to 14.7 meV and 4.2 meV, respectively [50], while it is similar to that found in organic electroluminescent (EL) materials, e.g. polydiacetylene (PDA) 0.5 eV, polythiophene (PT) 0.5 eV, CuPc 0.6 eV [51] and hBN 0.7 eV [52]. Nevertheless, the exciton binding energies for ZnS sheet are still smaller than the 2.1 eV in BN sheets and 1.6 eV in graphane, because the latter materials have much larger QP band gaps of 7.8 and 5.4 eV, respectively, [53-55] and thus less Coulomb screening. Experimental exciton binding energy for ZnS bulk is about 37 meV [56], which is smaller than exciton binding energy for ZnS sheet. This obviously shows that the dimensionality reduction of a ZnS sheet strongly confines the quasiparticles, and this quantum confinement with reduced screening (due to the presence of the vacuum region in the 2D system) significantly enhances the overlap between the electron and the hole wave functions and hence the electron-hole interaction. Our calculations show that the spectrum for 2D grapheme-like ZnS is dominated by strongly bound Frenkel excitons with a direct QP band gap.

Now, we calculate the effective mass and the Bohr radius of exciton for ZnS sheet. We used the same method used for graphene oxide [50]. The effective mass (μ) of the exciton in both bulk and sheet systems with a given binding energy was obtained by,

$$\mu = \frac{E_B}{R_h} \times \varepsilon_r^2 \times m_0 \qquad (10)$$

Where R_h is the Rydberg energy (13.6 eV), ε_r is dielectric constant and m_0 is the electron rest mass. The dielectric constants of ZnS sheet have been calculated from the real part of dielectric function within G_0W_0+BSE, GW_0+BSE and GW+BSE methods (Fig. 5 (b)) and are also given in Table 2. The effective masses found here ZnS sheet are smaller than that found in graphene oxide [50]. The exciton Bohr radius (a_x) can also be calculated with the following equation,

$$a_x = \frac{\varepsilon_r}{\mu} \times a_h \times m_0 \qquad (11)$$

where a_h is the Bohr radius (0.529 Å). Table 2 shows the present results of the exciton Bohr radius for ZnS sheet calculated by G_0W_0+BSE, GW_0+BSE and GW+BSE. Experimental exciton Bohr radius for ZnS bulk is about 24 Å [56], which is greater than that for ZnS sheet. It can be seen that the dimensionality reduction of a ZnS sheet decreases the exciton Bohr radius. In other words the smaller the Bohr radius leads to larger the binding energy. We can easily conclude that for a smaller radius, the electron and the hole will be confined in a narrower area, thus the e-h interaction is enhanced, and finally results in a larger binding energy.

The EELS function has been calculated in terms of real and imaginary parts of dielectric tensor, $\varepsilon_{\alpha\beta}(\omega)$, as defined by [8]

$$L_{\alpha\beta}(\omega) = -\mathrm{Im}\left(\frac{1}{\varepsilon_{\alpha\beta}(\omega)}\right) = \frac{\mathrm{Im}\,\varepsilon_{\alpha\beta}(\omega)}{\left(\mathrm{Re}\,\varepsilon_{\alpha\beta}(\omega)\right)^2 + \left(\mathrm{Im}\,\varepsilon_{\alpha\beta}(\omega)\right)^2} \qquad (12)$$

The EELS is useful in revealing plasma resonance phenomena as distinct from normal interband transitions. Fig. 6 illustrates the calculated EELS of ZnS sheet with three various approaches. Comparison of the EELS at the DFT+RPA and GW_0+RPA levels shows that when the self-energy corrections are included, the entire spectra have shifted to the high energy (blue-shift). On the other hand, GW_0+BSE yielded a red shift of EELS in comparison with GW_0+RPA. Furthermore, there is a large sharp peak in low frequencies at 4.35 eV for GW_0+BSE spectra, which were utterly missing in the DFT+GW_0 and GW_0+RPA. The Frenkel exciton is responsible for this low frequency peak of the π plasmon in the EELS. The second main peak for ZnS sheet appears at 7.23 eV which is related to $\pi+\sigma$ electron plasmon.

In the last step, we discuss the absorption coefficient *A (ω)* and the refraction index *n (ω)* of 2D-ZnS sheet. The absorption coefficient is obtained by using following relation:

$$A_{ij}(\omega) = \frac{\omega\,\mathrm{Im}\,\varepsilon_{ij}(\omega)}{c n_{ij}(\omega)} \qquad (13)$$

where $n_{ij}(\omega)$ is refraction index and it is given via the relation

$$n_{ij}(\omega) = \sqrt{\frac{\left|\varepsilon_{ij}(\omega) + \mathrm{Re}\,\varepsilon_{ij}(\omega)\right|}{2}} \qquad (14)$$

The absorption coefficient of 2D-ZnS sheet obtained using DFT+RPA, GW_0+RPA and GW_0+BSE has been plotted in Fig. 7 (a). When the self-energy corrections were included (GW_0+RPA), the entire absorption coefficient shifted to the high energy (blue shift), but when the e-h interactions were included (GW_0+BSE), the entire spectrum was pushed back. Thus, there is an obvious cancellation effect between the band-gap opening due to the quasi-particle corrections and the red shift of optical absorption due to the excitonic effects. It can be seen that the absorption edge of ZnS sheet is at 2.45 eV for DFT+RPA which has a blue shift by 2.15 eV for GW_0+RPA. The first absorption peak position for GW_0+BSE is evident at 4.26 eV, 0.34 eV lower than our results including the e-e interaction. The absorption coefficient of ZnS sheet reaches to its maximum value at about 6, 9 and 7 eV for DFT+RPA, GW_0+RPA and GW_0+BSE, respectively. Fig. 7 (b) illustrates the calculated refractive index of 2D-ZnS sheet structure using DFT+RPA, GW_0+RPA, and GW_0+BSE. The value of the static refraction index (the value of the refraction index at zero energy) in the ZnS sheet for parallel polarization is 1.41, 1.16 and 1.2 using DFT+RPA, GW_0+RPA, and GW_0+BSE, respectively. From the figure, one can observe that at energies about 6 eV for DFT+RPA, 9 eV for GW_0+RPA and 7 eV for GW_0+BSE, the refractive index is minimum, where the absorption is maximum.

4. Conclusions

In summary, we have employed state-of-the art many-body GWA and BSE approaches to study the QP band structure and optical properties of ZnS monolayer honeycomb structure. The QP band gaps of these systems have systematically been studied using various levels of GWA (G_0W_0, GW_0, and GW) constructed over PBE. Our results show that ZnS sheet has a direct gap at the Γ-point. However, GWA calculations at each three levels gave notably larger band gaps than calculations at PBE level; they keep unchanged the sort of direct semiconducting band gap in ZnS sheet. Finally, the optical properties of ZnS Sheet have been investigated at GW+BSE levels involving the inclusion of electron-hole correlation effects. Also, for a better understanding of optical properties of aforementioned systems, the optical property results of

DFT+RPA and GW+RPA have been reported. Comparison of the $\mathrm{Im}\,\varepsilon_{\alpha\beta}(\omega)$ obtained at the DFT+RPA and GW_0+RPA levels reveals that inclusion of electron-electron interaction led to a blue shift without changing the shape of the spectra. On the other hand, inclusion of electron-hole interaction in GW_0+BSE yielded a significant red shift of the $\mathrm{Im}\,\varepsilon_{\alpha\beta}(\omega)$. The first exciton peaks were evident at 3.86, 4.26, and 4.57 eV with large binding energy of 0.36, 0.49 and 0.73 eV using G_0W_0+BSE, GW_0+BSE and GW+BSE, respectively. Our results showed that the dimensionality reduction of a ZnS sheet decreases the exciton Bohr radius, while increases the binding energy. We showed that the spectrum of ZnS sheet is dominated by strongly bound Frenkel excitons. This strongly bound Frenkel exciton is also responsible for the low frequency peaks of the π plasmon in the energy loss function.

Acknowledgements

This work has benefited from a French government grant managed by ANR within the frame of the national program Investments for the Future ANR-11-LABX-022-01. The author would like to thank Dr. Alexander Mitrushchenkov for technical support and Prof. Céline Leonard for many helpful hints.

Reference

1. Schröer, P., P. Krüger, and J. Pollmann, *First-principles calculation of the electronic structure of the wurtzite semiconductors ZnO and ZnS.* Physical Review B, 1993. **47**(12): p. 6971-6980.

2. Reshak, A.H. and S. Auluck, *Ab initio calculations of the electronic, linear and nonlinear optical properties of zinc chalcogenides.* Physica B: Condensed Matter, 2007. **388**(1–2): p. 34-42.

3. Lashgari, H., et al., *Electronic and optical properties of 2D graphene-like ZnS: DFT calculations.* Applied Surface Science, 2016. **369**: p. 76-81.

4. J. Borah , K.S., *Optical and Optoelectronic Properties of ZnS Nanostructured Thin Film* Acta Physica Polonica A, 2008. **114**(4): p. 6.

5. Moradian, R. and M. Shahrokhi, *First principles study of the structural, electronic and optical properties of* $Zn_{1-x}Y_x$ *(Y= Cd, Mg) O nanotube.* Physica E: Low-dimensional Systems and Nanostructures, 2012. **44**(7–8): p. 1760-1765.

6. Harihar, B. and M. Gautam, *Tailoring the structural and electronic properties of a graphene-like ZnS monolayer using biaxial strain.* Journal of Physics D: Applied Physics, 2014. **47**(7): p. 075302.

7. Moradian, R. and M. Shahrokhi, *Structural, electronic and optical properties of* $Zn_{1-x}Sr_xO$ *nanotubes: First principles study.* Journal of Physics and Chemistry of Solids, 2013. **74**(8): p. 1063-1068.

8. Shahrokhi, M. and R. Moradian, *Structural, electronic and optical properties of* $Zn_{1-x}Zr_xO$ *nanotubes: first principles study.* Indian Journal of Physics, 2014. **89**(3): p. 249-256.

9. A. Esmailian, M.S., F. Kanjouri, *Structural, electronic and magnetic properties of (N, C)-codoped ZnO nanotube: First principles study.* Int. J. Mod. Phys. C 2015. **29**(11): p. 10.

10. Arghavani Nia, B., et al., *Density functional investigation of structural, electronic and magnetic properties of Cu-codoped ZnO nanotubes.* The European Physical Journal - Applied Physics, 2014. **67**(02): p. 20403 (7 pages).

11. Moradian, R., et al., *Fe nanochain and nanowires encapsulation in isolated finite thickness ZnO nanotube and its bundle systems.* Eur. Phys. J. Appl. Phys., 2014. **67**(2): p. 20406.

12. Peng, Q., et al., *Mechanical properties and stabilities of g-ZnS monolayers.* RSC Advances, 2015. **5**(15): p. 11240-11247.

13. Yamamoto, T., S. Kishimoto, and S. Iida, *Control of valence states for ZnS by triple-codoping method.* Physica B: Condensed Matter, 2001. **308–310**: p. 916-919.

14. Bredol, M. and J. Merikhi, *ZnS precipitation: morphology control.* Journal of Materials Science. **33**(2): p. 471-476.

15. Xu, C.N., et al., *Artificial skin to sense mechanical stress by visible light emission.* Applied Physics Letters, 1999. **74**(9): p. 1236-1238.

16. Calandra, P., M. Goffredi, and V.T. Liveri, *Study of the growth of ZnS nanoparticles in water/AOT/n-heptane microemulsions by UV-absorption spectroscopy.* Colloids and Surfaces A: Physicochemical and Engineering Aspects, 1999. **160**(1): p. 9-13.

17. Kennedy, T.A., et al., *Symmetry and electronic structure of the Mn impurity in ZnS nanocrystals.* Physical Review B, 1995. **52**(20): p. R14356-R14359.

18. Akhtar, M.S., et al., *Room temperature ferromagnetism and half metallicity in nickel doped ZnS: Experimental and DFT studies.* Materials Chemistry and Physics, 2015. **160**: p. 440-446.

19. Akhtar, M.S., et al., *Chemical bath deposition of Fe-doped ZnS thin films: Investigations of their ferromagnetic and half-metallic properties.* Materials Science in Semiconductor Processing, 2015. **39**: p. 283-291.

20. Akhtar, M.S., et al., *Structural, optical, magnetic and half-metallic studies of cobalt doped ZnS thin films deposited via chemical bath deposition.* Journal of Materials Chemistry C, 2015. **3**(26): p. 6755-6763.

21. Akhtar, M.S., et al., *Optimising conditions for the growth of nanocrystalline ZnS thin films from acidic chemical baths.* Materials Science in Semiconductor Processing, 2015. **30**: p. 292-297.

22. Fang, X., et al., *ZnS nanostructures: From synthesis to applications.* Progress in Materials Science, 2011. **56**(2): p. 175-287.

23. Li, L., et al., *Theoretical Insight into Faceted ZnS Nanowires and Nanotubes from Interatomic Potential and First-Principles Calculations.* The Journal of Physical Chemistry C, 2008. **112**(10): p. 3509-3514.

24. Behzad, S., et al., *Theoretical exploration of structural, electro-optical and magnetic properties of gallium-doped silicon carbide nanotubes.* Superlattices and Microstructures, 2014. **73**: p. 185-192.

25. Naderi, S., et al., *Structural, electronic and magnetic properties of Fe and Co monatomic nanochains encapsulated in BN nanotube bundle.* The European Physical Journal - Applied Physics, 2013. **62**(03): p. 30402 (6 pages).

26. Fathalian, A., R. Moradian, and M. Shahrokhi, *Optical properties of BeO nanotubes: Ab initio study.* Solid State Communications, 2013. **156**: p. 1-7.

27. Moradian, R., M. Shahrokhi, and S. Moradian, *First principle study of the structural, electronic and magnetic properties of Fe, Co, Ni atomic nanochains encapsulated in single walled and double walled beryllium oxygen nanotubes.* Physica E: Low-dimensional Systems and Nanostructures, 2013. **47**: p. 40-45.

28. Shahrokhi, M. and C. Leonard, *Quasi-particle energies and optical excitations of wurtzite BeO and its nanosheet.* Journal of Alloys and Compounds.

29. Krainara, N., et al., *Structural and electronic bistability in ZnS single sheets and single-walled nanotubes.* Physical Review B, 2011. **83**(23): p. 233305.

30. G. Mukhopadhyay, H.B., *Graphene and Some of its Structural Analogues: Full-potential Density Functional Theory Calculations.* World Journal of Engineering, 2013. **10**: p. 9.

31. Hohenberg, P. and W. Kohn, *Inhomogeneous Electron Gas.* Physical Review, 1964. **136**(3B): p. B864-B871.

32. Gajdoš, M., et al., *Linear optical properties in the projector-augmented wave methodology.* Physical Review B, 2006. **73**(4): p. 045112.

33. Shishkin, M. and G. Kresse, *Implementation and performance of the frequency-dependent GW method within the PAW framework.* Physical Review B, 2006. **74**(3): p. 035101.

34. Shishkin, M. and G. Kresse, *Self-consistent GW calculations for semiconductors and insulators.* Physical Review B, 2007. **75**(23): p. 235102.

35. Jiang, H., et al., *First-principles modeling of localized d states with the GW@LDA+U approach.* Physical Review B, 2010. **82**(4): p. 045108.

36. Salpeter, E.E. and H.A. Bethe, *A Relativistic Equation for Bound-State Problems.* Physical Review, 1951. **84**(6): p. 1232-1242.

37. Perdew, J.P., K. Burke, and M. Ernzerhof, *Generalized Gradient Approximation Made Simple.* Physical Review Letters, 1996. **77**(18): p. 3865-3868.

38. Kresse, G. and D. Joubert, *From ultrasoft pseudopotentials to the projector augmented-wave method.* Physical Review B, 1999. **59**(3): p. 1758-1775.

39. Kresse, G. and J. Furthmüller, *Efficient iterative schemes for ab initio total-energy calculations using a plane-wave basis set.* Physical Review B, 1996. **54**(16): p. 11169-11186.

40. Karlický, F. and M. Otyepka, *Band Gaps and Optical Spectra of Chlorographene, Fluorographene and Graphane from G_0W_0, GW_0 and GW Calculations on Top of PBE and HSE06 Orbitals.* Journal of Chemical Theory and Computation, 2013. **9**(9): p. 4155-4164.

41. Karlický, F. and M. Otyepka, *Band gaps and optical spectra from single- and double-layer fluorographene to graphite fluoride: many-body effects and excitonic states.* Annalen der Physik, 2014. **526**(9-10): p. 408-414.

42. Qiu, D.Y., F.H. da Jornada, and S.G. Louie, *Optical Spectrum of MoS_2: Many-Body Effects and Diversity of Exciton States.* Physical Review Letters, 2013. **111**(21): p. 216805.

43. Shahrokhi, M., S. Naderi, and A. Fathalian, *Ab initio calculations of optical properties of B_2C graphene sheet.* Solid State Communications, 2012. **152**(12): p. 1012-1017.

44. Moradian, R., et al., *Structural, magnetic, electronic and optical properties of iron cluster (Fe_6) decorated boron nitride sheet.* Physica E: Low-dimensional Systems and Nanostructures, 2012. **46**: p. 182-188.

45. Rohlfing, M. and S.G. Louie, *Electron-hole excitations and optical spectra from first principles.* Physical Review B, 2000. **62**(8): p. 4927-4944.

46. Dai, J. and X.C. Zeng, *Bilayer Phosphorene: Effect of Stacking Order on Bandgap and Its Potential Applications in Thin-Film Solar Cells.* The Journal of Physical Chemistry Letters, 2014. **5**(7): p. 1289-1293.

47. Fuchs, F., et al., *Efficient O(N2) approach to solve the Bethe-Salpeter equation for excitonic bound states.* Physical Review B, 2008. **78**(8): p. 085103.

48. Jiang, H., et al., *First-principles modeling of localized d states with the GW@LDA+U approach.* Physical Review B, 2010. **82**(4): p. 045108.

49. Shu, H., et al., *Quasi-particle energies and optical excitations of hydrogenated and fluorinated germanene.* Physical Chemistry Chemical Physics, 2015. **17**(6): p. 4542-4550.

50. Lee, D., et al., *Quantum confinement-induced tunable exciton states in graphene oxide.* Scientific Reports, 2013. **3**: p. 2250.

51. Knupfer, M., *Exciton binding energies in organic semiconductors.* Applied Physics A, 2003. **77**(5): p. 623-626.

52. L. Wirtz, A.M., M. Gruning, A. Rubio, *Excitonic effects in optical absorption and electron-energy loss spectra of hexagonal boron nitride.* arXiv:cond-mat/0508421, 2005.

53. Luo, G., et al., *Quasiparticle energies and excitonic effects of the two-dimensional carbon allotrope graphdiyne: Theory and experiment.* Physical Review B, 2011. **84**(7): p. 075439.

54. Wirtz, L., A. Marini, and A. Rubio, *Excitons in Boron Nitride Nanotubes: Dimensionality Effects.* Physical Review Letters, 2006. **96**(12): p. 126104.

55. Cudazzo, P., et al., *Strong Charge-Transfer Excitonic Effects and the Bose-Einstein Exciton Condensate in Graphane.* Physical Review Letters, 2010. **104**(22): p. 226804.

56. Yamada, Y., et al., *Optical properties of biexcitons in ZnS.* Physical Review B, 2000. **61**(12): p. 8363-8368.

Table 1. The energy band gap (eV) values of 2D graphene-like ZnS calculated by PBE, G_0W_0, GW_0 and GW approaches. The present results are compared with previous theoretical data.

Method	Band gap (eV)
Present results	
PBE	2.65
G_0W_0	4.22
GW_0	4.75
GW	5.30
Other theoretical works	
LDA [29]	2.62
GGA [3]	2.77
GGA-EV [3]	3.01

Table 2. Exciton energies (E_{ex}), lowest exciton binding energy (E_B), static dielectric constant (ε_r), exciton effective mass (μ) and exciton Bohr radius (a_x) of ZnS graphen-like sheet calculated by G_0W_0+BSE, GW_0+ BSE and GW+ BSE approaches.

Method	E_{ex} (eV)			E_B (eV)	ε_r	μ (m_0)	a_x (Å)
	E_0^{11}	E_1^{11}	E_2^{11}				
G_0W_0+BSE	3.86	4.60	4.95	0.36	1.56	0.064	12.89
GW_0+BSE	4.26	4.99	5.36	0.49	1.45	0.075	10.23
GW+BSE	4.57	5.27	5.64	0.73	1.39	0.104	7.07

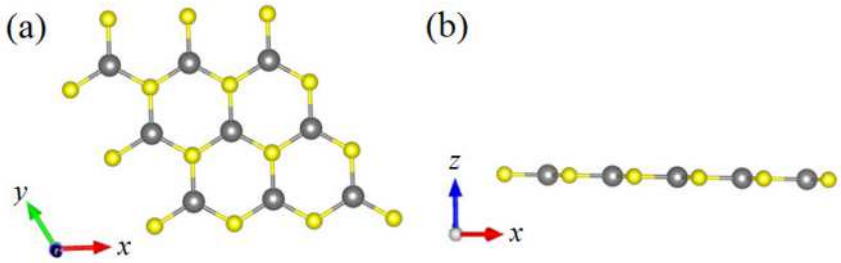

Fig. 1. Top (a) and side views (b) of the graphene-like 2D-ZnS. Big gray and small yellow balls in geometrical models represent zinc and sulphide atoms, respectively.

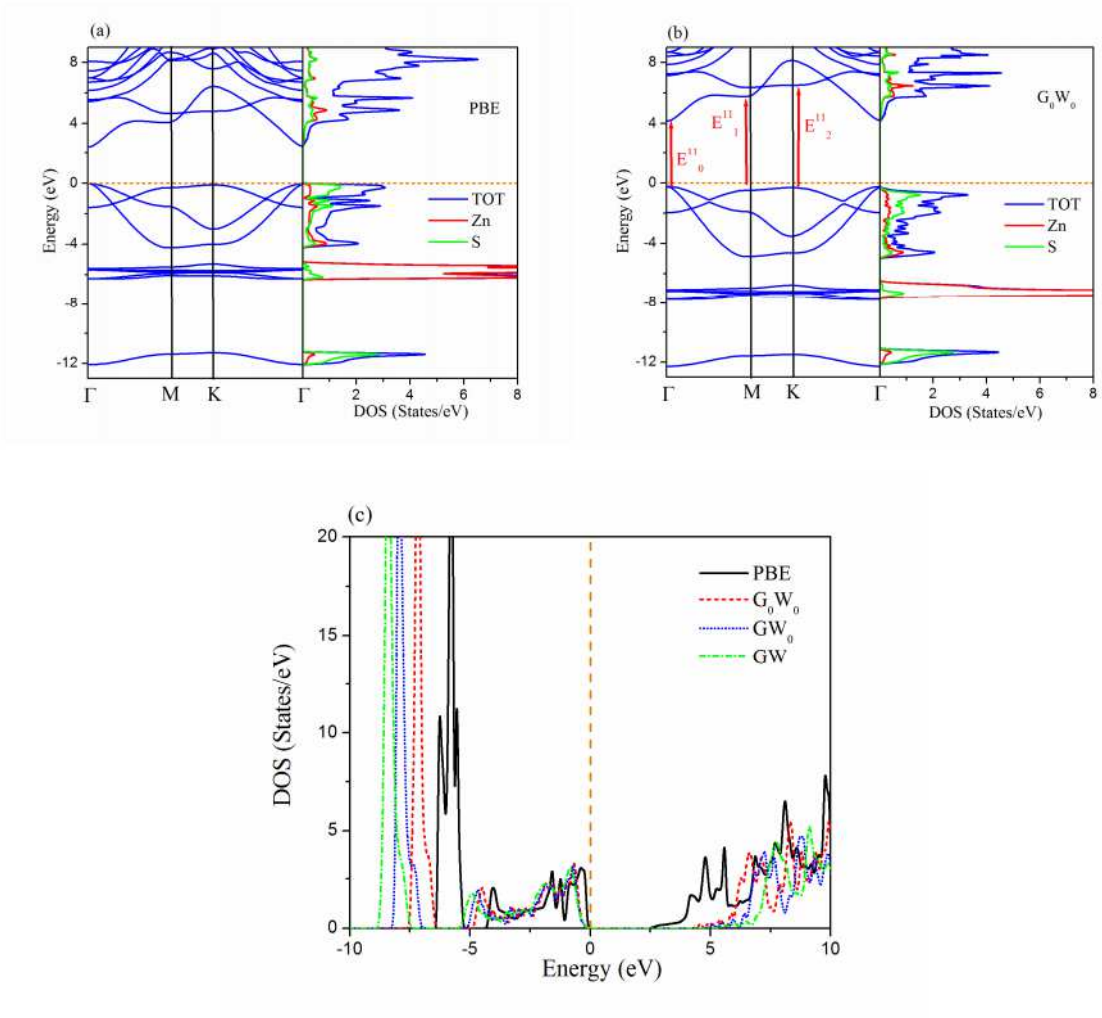

Fig. 2. Band structure, total and partial DOS of 2D graphene-like ZnS calculated with (a) PBE and (b) G_0W_0. The red arrows indicate the lowest optical transitions taking place in the systems.

(c) Total density of states of 2D graphene-like ZnS using the PBE (black line), G_0W_0 (red dashed line), GW_0 (blue dotted line) and GW (green dash-dotted line). The Fermi energy is aligned to zero.

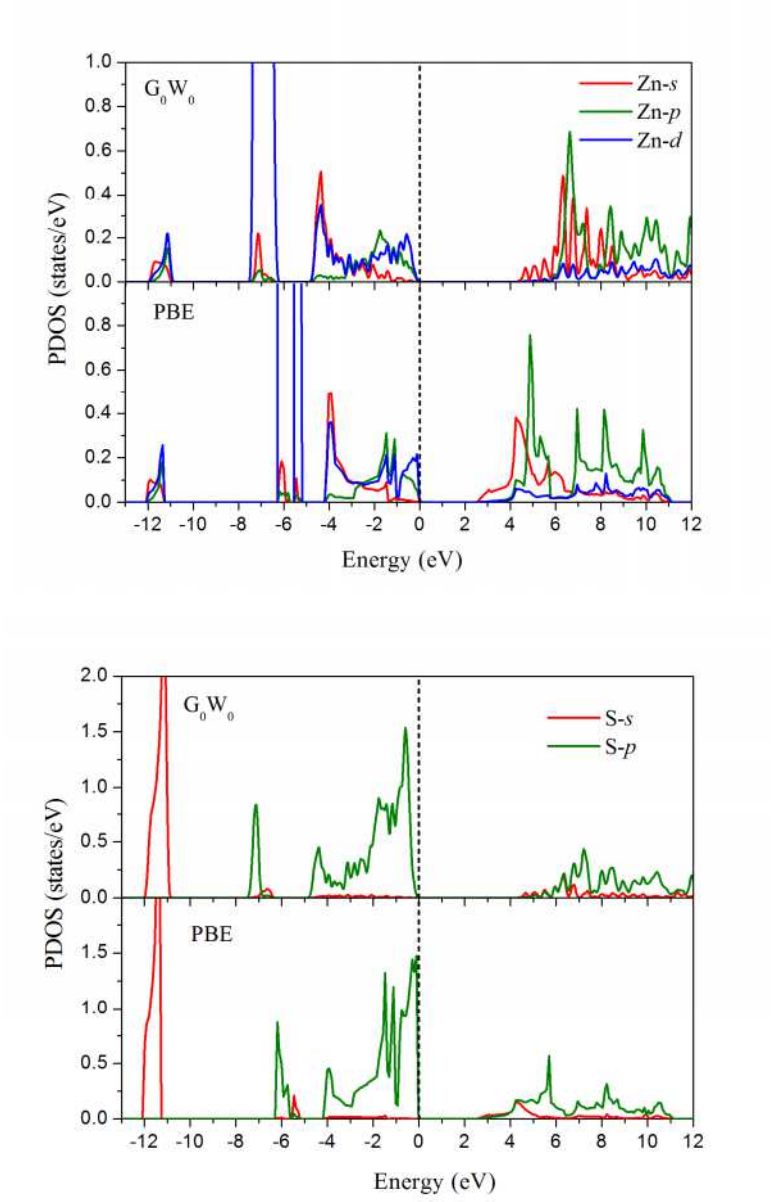

Fig. 3. The partial DOS of 2D graphene-like ZnS calculated with PBE and G_0W_0. The Fermi energy is aligned to zero.

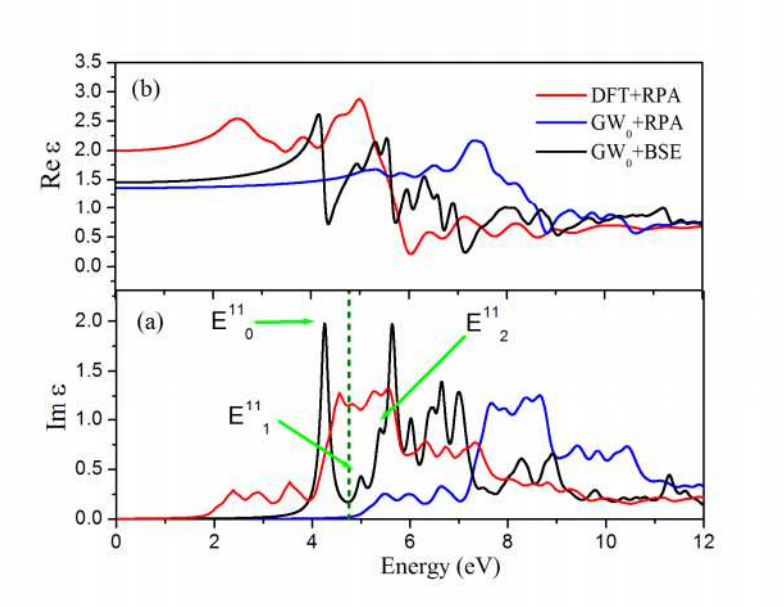

Fig. 4. (a) Imaginary part and (b) real part of dielectric function of ZnS graphen-like sheet using the DFT+RPA (red line), GW_0+RPA (blue line) and GW_0+BSE (black line) for light polarization parallel to the surface plane. Green dashed line is GW_0 band gap.

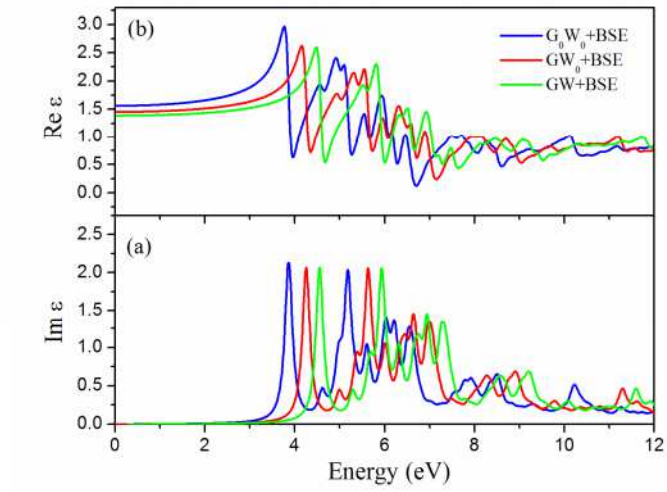

Fig. 5. (a) Imaginary part and (b) real part of dielectric function of ZnS graphen-like sheet using the G_0W_0+BSE (blue line), GW_0+BSE (red line) and GW+BSE (green line) for light polarization parallel to the surface plane.

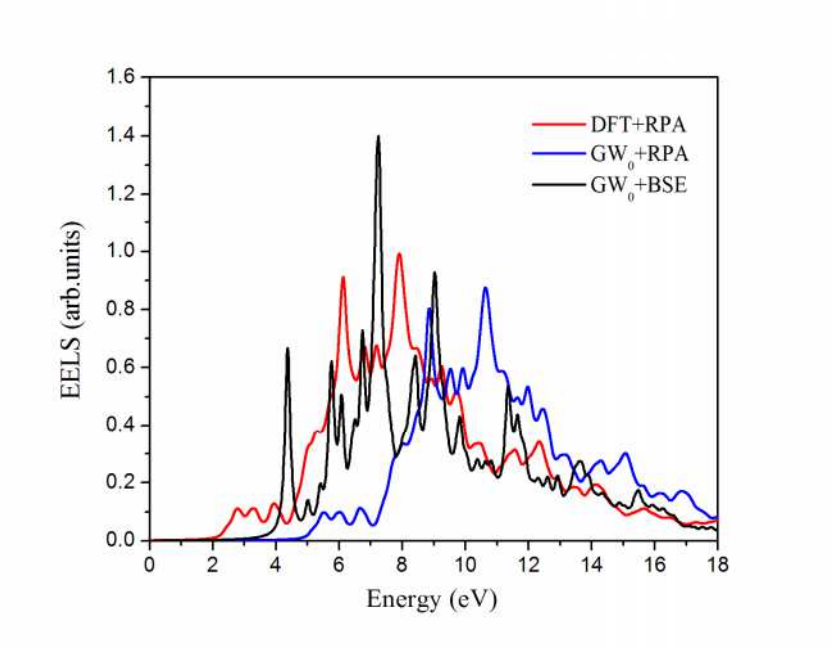

Fig. 6. Calculated loss function of ZnS graphen-like sheet using the DFT+RPA (red line), GW_0+RPA (blue line) and GW_0+BSE (black line) for light polarization parallel to the surface plane.

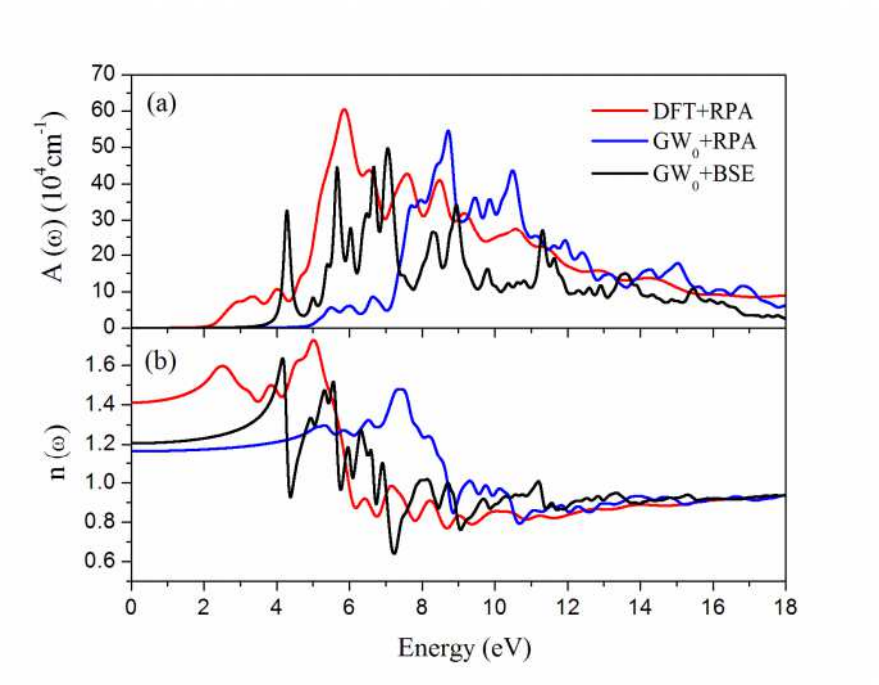

Fig. 7. Calculated (a) absorption coefficient *A (ω)* and (b) refraction index *n (ω)* of ZnS graphen-like sheet using the DFT+RPA (red line), GW_0+RPA (blue line) and GW_0+BSE (black line) for light polarization parallel to the surface plane.